Interactive annular mode links jet stream-ocean coupling to decadal Northern Hemispheric warmth

TSUBASA KOHYAMA*, YOKO YAMAGAMI, SHOICHIRO KIDO,
FUMIAKI OGAWA, HIROAKI MIURA

Department of Information Sciences, Ochanomizu University, Tokyo, Japan
Japan Agency for Marine-Earth Science and Technology, Yokohama, Japan
Faculty of Bioresources, Mie University, Tsu, Japan
Department of Earth and Planetary Science, The University of Tokyo, Tokyo, Japan

ABSTRACT

The atmospheric jet stream governs the distribution and intensity of midlatitude weather systems and climate variability. In the Northern Hemisphere, meridional migrations of the jet stream are directly linked to the frequency and magnitude of extreme weather events. While previous studies have established that jet stream fluctuations are modulated by spatio-temporal variations in diabatic heating, the relationship between low-frequency modes of atmospheric and oceanic variability remains unclear. Here we propose a hypothesis that the Northern Annular Mode (NAM) and the Pacific Decadal Variability (PDV), the most dominant modes of climate variability in the Northern Hemisphere, constitute an annular-shaped air-sea coupled mode. The singular value decomposition analysis of sea surface temperatures and lower tropospheric zonal winds shows that the most dominant covariability over the Northern Hemisphere closely corresponds to both the conventional PDV and NAM patterns. The extracted PDV-like and NAM-like modes explain 46% of each other's variance, suggesting substantial coupling, and we refer to this hypothesized air-sea coupled phenomenon as the interactive Annular Mode (iAM). We detect a positive feedback mechanism that amplifies iAM to be a dominant mode by conducting a heat budget analysis and performing a pacemaker experiment with a high-resolution global climate model. The record-breaking heat waves observed across the Northern Hemisphere in 2024 are attributed to recent prolonged positive phase of iAM.

1. Introduction

The jet stream, a band of strong westerly winds in the atmosphere, plays a crucial role in determining weather and climate in the midlatitudes (e.g., Shapiro and Keyser 1990; Holton and Hakim 2013; Hartmann 2015). In particular, in the Northern Hemisphere, the meridional position of the jet stream has a profound impact on extreme weather (e.g., Barnes 2013; Screen and Simmonds 2014; Cohen et al. 2021). As the most recent example, Fig. 1a shows that the jet stream experienced an unusually northward displacement during boreal summer in 2024 relative to its typical position. Concurrently, many densely-populated cities across the Northern Hemisphere experienced severe heat waves (*see also* Fig. 5c), contributing to the unprecedented global-mean temperature observed in 2024 (Lenssen et al. 2024; GISTEMP Team 2025; Vlock and Jacobs 2025). The combination of anthropogenic greenhouse gas-forced temperature rise and poleward fluctuations of the jet stream poses severe risks to human society (e.g., Masson-Delmotte et al. 2021). These risks include increased heat-related mortality (Honda et al. 2014; Gasparrini et al. 2015), agricultural disruption (Lobell et al. 2011; Ray et al. 2019), and strain on critical infrastructure (Chester et al. 2019).

The most dominant mode of atmospheric variability regarding the meridional fluctuations of the jet stream is referred to as the Northern Annular Mode (NAM) or the Arctic Oscillation (AO) (Thompson and Wallace 1998, 2001). During the positive phase of NAM, the strengthened jet stream shifts northward and forms a circular pattern around the North Pole, which confines cold air within the polar regions. By contrast, during the negative NAM, the weakened jet stream shifts southward and becomes distorted, which allows cold Arctic air to move southward more frequently, enhancing the storm track activity in the midlatitudes. The fundamental importance of NAM in Northern Hemispheric atmospheric variability has led to extensive research on its amplitude, phase, and response to climate change (e.g., Limpasuvan and Hartmann 2000; Wallace 2000; Kimoto et al. 2001; Watanabe and Jin 2004;

*Corresponding author address: Department of Information Sciences, Ochanomizu University, 2-1-1, Bunkyo-ku, Tokyo, Japan, 112-8610
E-mail: tsubasa@is.ocha.ac.jp

Generated using v4.3.2 of the AMS LaTeX template

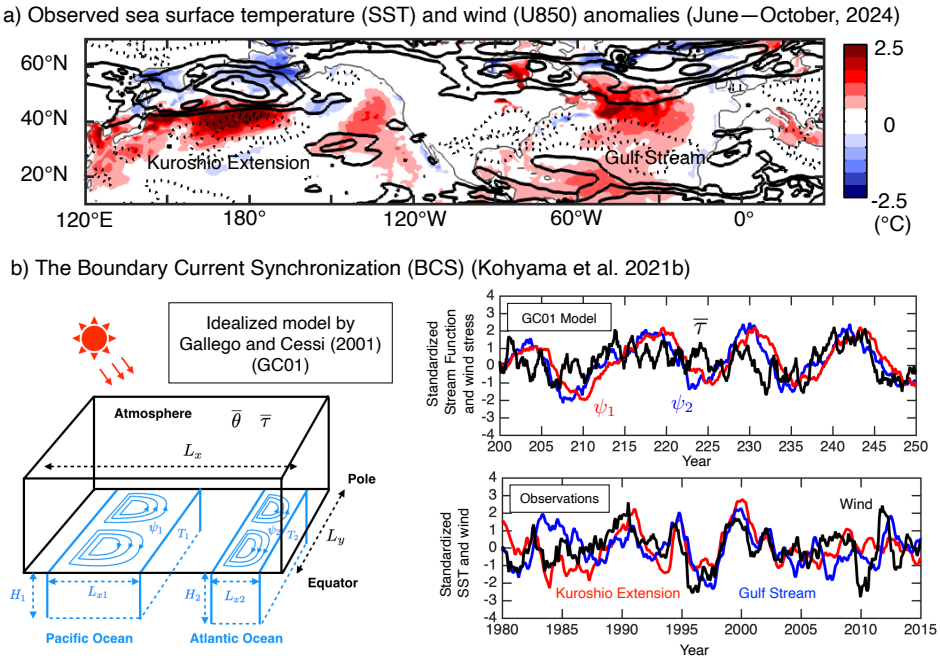

FIG. 1. **Northward displacement of the jet stream and its association with the midlatitude ocean.** (a): Observed sea surface temperature (SST) (shaded areas) and zonal wind at 850 hPa (U850) (contours) averaged from June through October of 2024. Contour interval is 0.6 m/s, and zero contours are omitted. (b): Summary of the Boundary Current Synchronization (BCS). Left, Schematic diagram of the idealized model formulated by Gallego and Cessi (2001) (GC01). Top right, Stream function anomalies ψ_1 (red) and ψ_2 (blue) at 4,000 km north of the southern boundary of the GC01 idealized model. Also shown in black is zonal-mean westerly wind stress ($\overline{\tau}$) anomalies at 5,200 km north of the equator. Bottom right, Observed SST anomaly time series averaged over the Gulf Stream (35°N-45°N, 80°W-50°W) (blue) and the Kuroshio (35°N-45°N, 140°E-170°E) (red) regions. Also shown in black is observed zonal wind at 850 hPa averaged over the Northern Pacific and Atlantic (45°N-60°N, 140°E-0°). One-year running-mean filtering is applied, and normalized by its own standard deviation. Figures from the final published version are reproduced from Kohyama et al. (2021b) with permissions by *Science*.

Ring and Plumb 2007; Gillett and Fyfe 2013; Omrani et al. 2019), and sparked a debate about its distinguishability from the North Atlantic Oscillation (e.g., Ambaum et al. 2001; Deser 2000).

The accumulated wisdom of climate dynamics has established that the jet stream position has a strong association with diabatic heating, which originates from atmospheric radiation and phase transitions of water. Horel and Wallace (1981) and Rasmusson and Wallace (1983) demonstrated that moist convective heating associated with sea surface temperature (SST) variability in the tropical Pacific influences the midlatitude jet stream position through a stationary Rossby wave response. This atmospheric process is now known as the Pacific-North American (PNA) teleconnection. Hoskins and Valdes (1990) suggested that the uneven distribution of diabatic heating in the midlatitudes, particularly due to the non-uniformity of SST created by western boundary currents (strong warm ocean currents along the western boundaries of the world's major ocean basins), determines the favorable locations of storm tracks and jet stream positions.

Research on western boundary currents has further revealed their crucial role in modulating atmospheric conditions. SST variations associated with western boundary current dynamics influence local weather through heat transport from the tropics to the midlatitudes (e.g., Sanders 1986; Young and Sikora 2003). High-resolution satellite observations have revealed that heat release from western boundary currents affects the entire tropospheric layer (Minobe et al. 2008; Nakamura et al. 2015; Masunaga et al. 2018). These findings provide context for understanding the most recent event: the abnormally high SSTs observed in the midlatitude ocean during boreal summer 2024 (Fig. 1a), and their associated anomalous oceanic heat release, may have contributed to the observed northward shift of the jet stream.

In fact, recent research has unveiled their planetary-scale cooperative behavior of western boundary currents, and their association with the atmospheric jet stream. Based on observational analyses and high-resolution climate model simulations, Kohyama et al. (2021b) discovered that SSTs of the Gulf Stream and the Kuroshio Extension, the two major western boundary current regions

in the Northern Hemisphere, are synchronized at interannual to decadal time scales. This phenomenon, termed the Boundary Current Synchronization (BCS), is associated with meridional migrations of the jet stream. Furthermore, building upon a toy model by Gallego and Cessi (2001), Kohyama et al. (2021b) constructed a conceptual model and explained BCS as an air-sea coupled oscillatory system, in which two western boundary currents are connected by zonally-symmetric atmosphere (Fig. 1b). By applying recent advances in information thermodynamics, Yasuda and Kohyama (2025) demonstrated that information transfer via the jet stream plays a key role in BCS dynamics. Additionally, climate modeling work by Yamagami et al. (2025) revealed a physical mechanism for information flow from the Gulf Stream to the Kuroshio Extension through NAM-like atmospheric variability and its excitation of oceanic Rossby waves. Dong et al. (2025) also discussed that the Pacific Decadal Variability (PDV) (Minobe 1997; Mantua et al. 1997) emerges as the large-scale modulator of co-occurring summertime marine heatwaves in the extratropical North Pacific and Atlantic.

The zonally-symmetric nature of jet stream variability associated with BCS implies that low-frequency NAM variance could be understood as an air-sea coupled mode amplified by interactions with interannual to decadal scale SST variability in western boundary current regions. While midlatitude SST variations are often interpreted as signatures of dominant natural modes of variability—such as PDV and the Atlantic Meridional Overturning Circulation (Zhang 2008)—examining them through the lens of ocean-atmosphere interactions provides new insights. Reconstructing our understanding of atmospheric annular modes and oceanic decadal variability holds the key to advancing fundamental climate dynamics and inform paleoclimatology (Yamamoto et al. 2004), climate modeling (Paul and Schäfer-Neth 2003), and future climate change projections (Wills et al. 2018).

Hence, in this study, we hypothesize that the low-frequency component of conventional NAM and PDV constitutes an air-sea coupled system, and present results that coherently substantiate it. Section 2 presents our data and methods. In Section 3, we demonstrate that the singular value decomposition (SVD) analysis reveals a dominant low-frequency covariability between conventional NAM and PDV. Section 4 shows that this covariability can be interpreted as an air-sea coupled annular mode and discusses its implications for the record-breaking heat waves observed in 2024. We present our conclusions in Section 5.

2. Data and Methods

a. Observational and reanalysis products

Observed SST data are obtained from the National Oceanic and Atmospheric Administration (NOAA) Optimum Interpolation SST (OISST) version 2 High Resolution Dataset (Huang et al. 2021) available at `https://www.esrl.noaa.gov/psd/data/gridded/data.noaa.oisst.v2.highres.html`. Observed zonal wind field at 850 hPa are derived from the European Center for Medium range Weather Forecasting (ECMWF) reanalysis version 5 (ERA-5) data (Hersbach et al. 2020) available at `https://cds.climate.copernicus.eu/datasets/reanalysis-era5-pressure-levels-monthly-means?tab=download`. For computational efficiency, these observational data are regridded to 1° resolution in both longitude and latitude.

The conventional monthly-mean NAM index (also known as the AO index) and PNA index are downloaded from the Climate Prediction Center (`https://www.cpc.ncep.noaa.gov/products/precip/CWlink/daily_ao_index/teleconnections.shtml`). The conventional PDV index (also known as the Pacific Decadal Oscillation index) is from the NOAA National Centers for Environmental Information (`https://www.ncei.noaa.gov/access/monitoring/pdo/`). Essentially, the conventional NAM and PDV index is calculated as the leading principal component (PC) of 1,000 hPa geopotential height over the Northern Hemisphere and the Pacific SST, respectively, poleward of 20°N. The PNA index is obtained as one of the ten dominant rotated PC modes of 500 hPa geopotential height anomalies poleward of 20°N. For further details, readers are referred to the websites listed above. In addition, following Kohyama et al. (2021b), the BCS index is defined as the average of regional-mean SST anomalies over the Gulf Stream (35°N-45°N, 80°W-50°W) and the Kuroshio Extension (35°N-45°N, 140°E-170°E) regions.

Sea-level elevation and surface heat flux is based on the Japan Coastal Ocean Predictability Experiments-Forecasting Global Ocean (JCOPE-FGO), an eddy-resolving quasi-global ocean reanalysis product (Kido et al. 2022), whose horizontal resolution is 0.1°. Geostrophic ocean current is calculated from sea-level elevation, and geostrophic thermal advection at the surface is estimated as dynamical temperature advection by geostrophic currents: $-\overline{u_g}(\partial T'/\partial x) - u_g'(\partial \overline{T}/\partial x) - \overline{v_g}(\partial T'/\partial y) - v_g'(\partial \overline{T}/\partial y) - u_g'(\partial T'/\partial x) - v_g'(\partial T'/\partial y)$. Here, u_g and v_g are geostrophic currents in the x (zonal) and y (meridional) directions, respectively, and T represents SST; overlines denote climatology (means of each calendar month), and primes indicate deviations from climatology.

The analysis period spans from 1982 through 2024 for most observational products, except for the JCOPE-FGO data, which are available from 1993 through 2023 at the time of analysis (used to make Figs. 4d and 4e).

b. Pacemaker model experiment

The global climate model employed in this study is an eddy-permitting configuration of the Model for Interdisciplinary Research on Climate version 6 (MIROC6subhires) (Tatebe et al. 2019). The atmospheric and land surface components of MIROC6subhires utilize a horizontal resolution of the T85 spectral truncation. The model comprises 81 vertical levels with the top of the atmosphere at 0.004 hPa. The ocean and sea ice components employ a tripolar horizontal coordinate system with a nominal resolution of 0.25° and 62 vertical levels. Following the protocol of the Coupled Model Intercomparison Project Phase 6 (CMIP6) (Eyring et al. 2016), MIROC6subhires was spun up for 700 years using preindustrial external forcing. After reaching a quasi-equilibrium state, the model was integrated for an additional 200 years. The final 100 years of this integration serve as the preindustrial control run, which is utilized as described in the following paragraph.

In Section 4, we analyze output from a high-resolution pacemaker experiment, wherein SSTs in the two boundary current regions were constrained by SST output from the preindustrial control run. Outside these boundary current regions, the fully-coupled atmosphere and ocean evolved freely. These experimental configurations are essentially identical to the eddy-permitting western boundary current pacemaker experiments with MIROC6subhires conducted by Yamagami et al. (2025), except that the SST restoring area encompassed both the Gulf Stream and Kuroshio Extension regions rather than a single region. The experiment generated 100-year pacemaker simulations with eddy-permitting resolution for five ensemble members initialized with different conditions. To ensure independent decadal variability among simulations, we selected these initial conditions from the preindustrial control run with time separations exceeding 10 years. The ensemble mean of these five members minimizes natural variability not originating from the western boundary current regions. For detailed experimental configurations, readers are referred to Yamagami et al. (2025).

For the atmospheric analysis, we utilize zonal wind output at 300 hPa instead of 850 hPa, as the latter is undefined over mountainous regions in the model, unlike in reanalysis products. The qualitative features revealed by the regression analyses are not sensitive to this choice of pressure level, owing to the equivalent barotropic nature of the investigated phenomenon.

c. Analysis Methods

We analyze detrended monthly anomalies obtained by removing monthly climatology and linear trends, except for Fig. 5a, where the linear trend is retained. The statistical significance of correlations is assessed using the two-tailed Student's t-test. To account for autocorrelation in the time series when estimating statistical degrees of freedom, we employ the formula proposed by Bretherton et al. (1999). For one-year low-pass filtering in Figs. 3, 4d, and 4e, the first-order Butterworth filter is applied.

3. The most dominant covariability between SST and zonal wind

In this section, we examine the most dominant covariability between midlatitude ocean and atmosphere in the Northern Hemisphere, focusing on the first mode of SVD (SVD1) between SST and lower tropospheric zonal wind. In particular, we demonstrate that this mode exhibits essential characteristics of both conventional PDV and NAM, which serves as one of the strong pieces of evidence for the hypothetical coupling between these leading modes of climate variability.

a. PDV-like and NAM-like modes extracted as SVD1

To extract the dominant ocean-atmosphere covariability, we perform SVD analysis (also known as Maximum Covariance Analysis) on SST and zonal wind anomalies over the North Pacific-Atlantic region (35°N-55°N, 120°E-0°). The analysis domain is chosen to focus on midlatitude dynamics where ocean-atmosphere coupling is expected to be strongest. The spatial pattern of SVD1 (Fig. 2a) exhibits a PDV-like SST variability and a NAM-like zonal wind variability. Although the tropics is not drawn in Fig. 2a, the SVD signals are largely confined to midlatitudes. The two SVD1 time series, obtained by projecting the original anomalies onto these spatial patterns (Fig. 2d, red and blue solid curves), share 48% of their variance (reflecting a correlation of $r = 0.69$), indicating a robust covariability rather than random coincidence.

SVD1 represents a shared mode of variability between PDV and NAM. The SVD1 SST time series shows a significant correlation of 0.71 with the conventional PDV index (sign reversed) (Fig. 2d, red), while the zonal wind time series shows a significant correlation of 0.72 with the NAM index (Fig. 2d, blue). Spatially, SVD1 (Fig. 2a) exhibits enhanced zonal wind signals over the Atlantic compared to the conventional PDV pattern (Fig. 2b), and stronger SST signatures in the North Pacific than typically associated with NAM (Fig. 2c).

While SVD1 captures essential aspects of both PDV and NAM, we acknowledge that it may not encompass all components of these modes. For instance, previous studies have demonstrated that PDV comprises both internal variability and tropically-forced components (e.g., Newman et al. 2016; Zhang et al. 2018). Our analysis focuses specifically on the internal component driven by midlatitude dynamics. Similarly, for NAM, we primarily address its low-frequency component, as high-frequency NAM variations are well-reproduced even with prescribed climatological SST (Limpasuvan and Hartmann 2000).

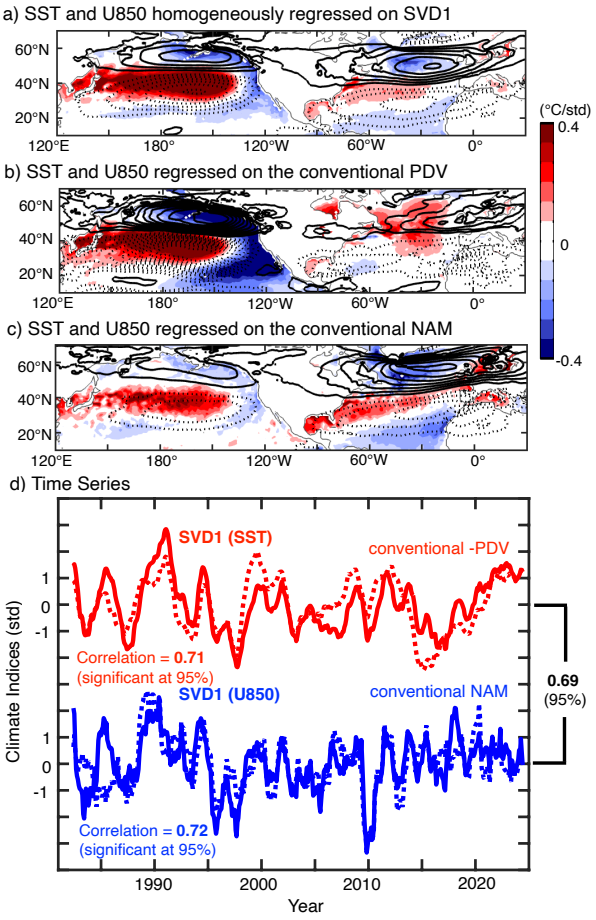

FIG. 2. **The most dominant covariability between SST and zonal wind.** (a): Homogeneous regression maps of SST (shaded areas) and U850 (contours) onto the first mode of the singular value decomposition (SVD1) time series between SST and U850 performed over over the north Pacific-Atlantic region (35°N-55°N, 120°E-0°). Contour interval is 0.6 m/s, and zero contours are omitted. (b): As in (a), but for the conventional Pacific Decadal Variability (PDV) index (sign reversed). Contour interval is 0.1 m/s. (c): As in (a), but for the conventional Northern Annular Mode (NAM) index. (d) Solid, SVD1 time series obtained by projecting SST (red) and U850 (blue) onto their corresponding SVD1 singular vector. One-year running-mean filtering is applied, and normalized by its own standard deviation. Dashed, As in the solid curves, but for the conventional PDV (sign reversed) (red) and NAM (blue) indices.

b. The relationship between SVD1 and known modes of climate variability

PDV and NAM have traditionally been defined through statistical methods as the leading principal components (PCs) of SST and geopotential height fields, respectively. While these statistical definitions have proven useful, they may not fully correspond to physically meaningful modes of variability. Indeed, when extracting physical modes solely through statistical analyses, inherent arbitrariness remains in several aspects, including but not limited to the choice of physical variables to analyze, the definition of spatial domains, and the selection of statistical methods.

To address this limitation and better understand the physical significance of SVD1, we examine its relationship with these conventional modes by mapping them in the phase space defined by the leading PCs (Fig. 3a). These PCs are computed separately for Northern Hemispheric SST and zonal wind (north of 20 ° N), with both datasets subjected to one-year low-pass filtering. It is important to clarify that the PC1 of SST, PC2 of SST, PC1 of zonal wind, and PC2 of zonal wind represent different statistical modes of variability. This approach allows us to evaluate how SVD1 relates to established climate patterns within a unified statistical framework.

For SST, PC1 primarily reflects tropical influences, while PC2 highlights SST front variability mainly in the North Pacific (Fig. 3a, top). Following Quadrelli and Wallace (2004), we project various climate indices (one-year low-pass filtered) onto this PC1-PC2 phase space (Fig. 3b, top). On this diagram, if a point representing a mode is close to the unit circle, it means that the variance of this particular mode can mostly be explained by a linear combination of PC1 and PC2. The SVD1 SST pattern appears as approximately a 45° rotation of the conventional PDV toward PC2, with its proximity to the unit circle confirming its status as a dominant mode in the Northern Hemisphere. At the same time, SVD1 explains the qualitative feature of PDV, as shown in Fig. 2, because SVD1 is located close enough to PDV in the phase space. In addition, the BCS index (Kohyama et al. 2021b), which is defined as SST anomalies averaged over the Gulf Stream and Kuroshio Extension regions, turns out to be one of the nearest neighbors of SVD1, suggesting that BCS is a fundamental feature of this SVD mode.

In the zonal wind field, PC1 resembles an annular mode structure, while PC2 reflects tropical teleconnection patterns (Fig. 3a, bottom). The phase space analysis (Fig. 3b, bottom) reveals that the SVD1 zonal wind pattern represents approximately a 40° rotation of NAM toward the PNA pattern. Its position near the unit circle again confirms its significance as a dominant mode of Northern Hemisphere variability. Interestingly, the difference between NAM and PNA indices closely corresponds to the SVD1 position.

While SVD1 differs somewhat from conventional definitions of dominant climate modes, our analysis demonstrates that it can be expressed as a linear combination of the two leading PCs, confirming its fundamental dominance in nature. At the same time, when focusing on the covariance between SST and zonal wind, SVD1 is the most important mode by definition. In the following section, we will further elucidate the characteristics and physical processes of this dominant covariability extracted as SVD1.

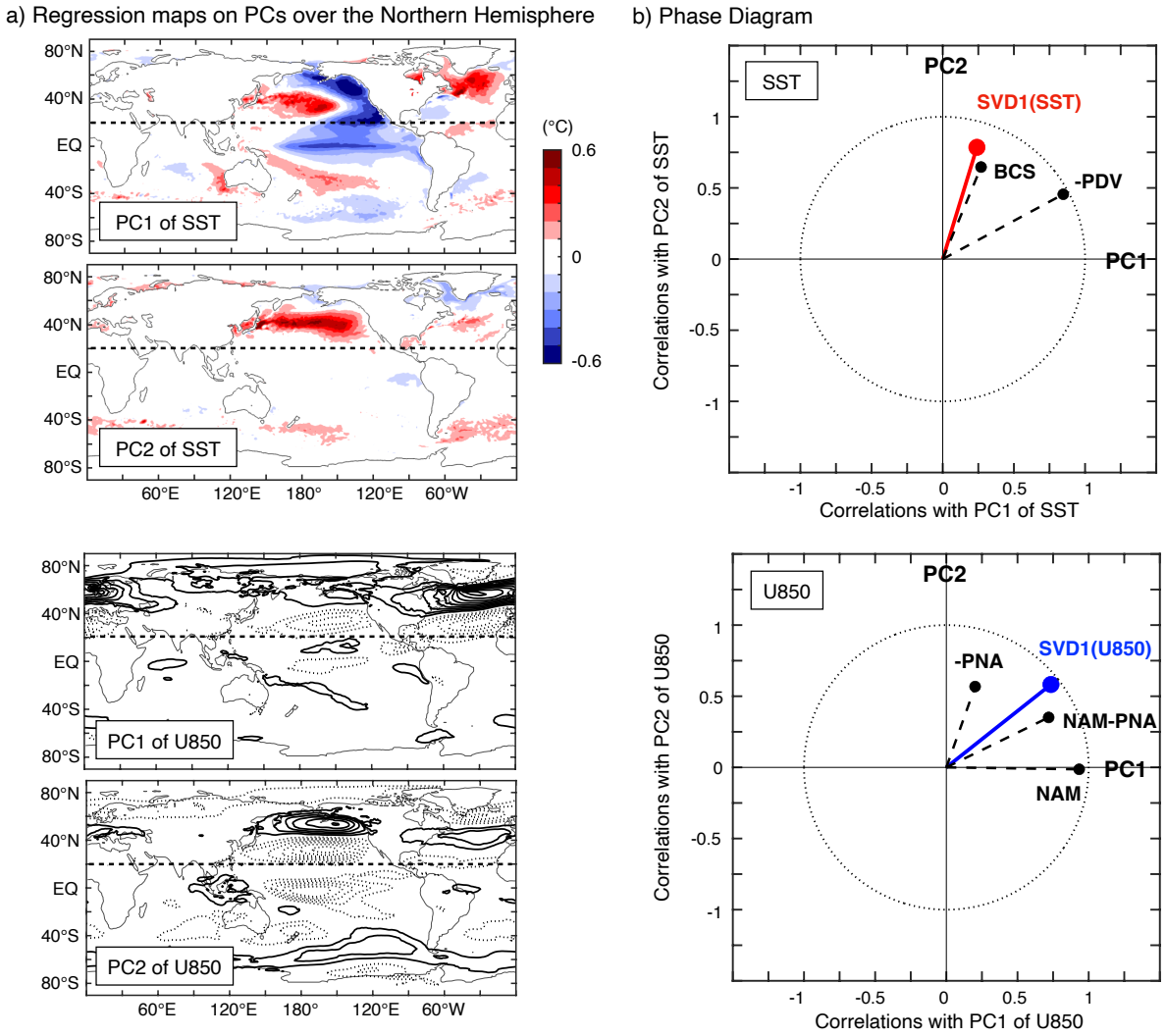

FIG. 3. **The relationship between SVD1 and known modes of climate variability.** (a): Regression maps of SST (top) and U850 (bottom) onto the first and second modes of the principal component (PC) time series (one-year low-pass filtered) performed for the Northern Hemisphere (north of 20°N indicated as solid dashed line). Contour interval is 0.2 m/s, and zero contours are omitted. (b): Projections of various indices on the phase space defined by the two leading PCs of SST (top) and U850 (bottom). Temporal correlations between one-year low-pass filtered indices and the PC time series are plotted. Positive values of the PCs denote polarities indicated in (a), and the negative sign indicate that the sign is reversed from the conventional index. See Quadrelli and Wallace (2004) for more details of the methodology.

4. The interactive Annular Mode (iAM)

The results presented in the previous section reveal a fundamental connection between PDV and NAM that is more direct than previously recognized. This finding motivates an investigation into an internal air-sea coupled mode that accounts for substantial low-frequency variability in both phenomena. The prevalence of such coupled modes in midlatitudes can be supported by the relatively slow oceanic baroclinic Rossby wave propagation in the midlatitudes (Chelton and Schlax 1996), which implies longer characteristic timescales than those of tropical phenomena such as the El Niño Southern Oscillation (ENSO).

Based on this motivation, we propose the existence of a natural mode of variability—termed the interactive Annular Mode (iAM)—that is maintained through ocean-atmosphere interactions. This section establishes optimal indices to characterize iAM and examines the physical mechanisms underlying its dominance in midlatitude climate variability through heat budget analysis and a global climate model experiment. Finally, we further explore

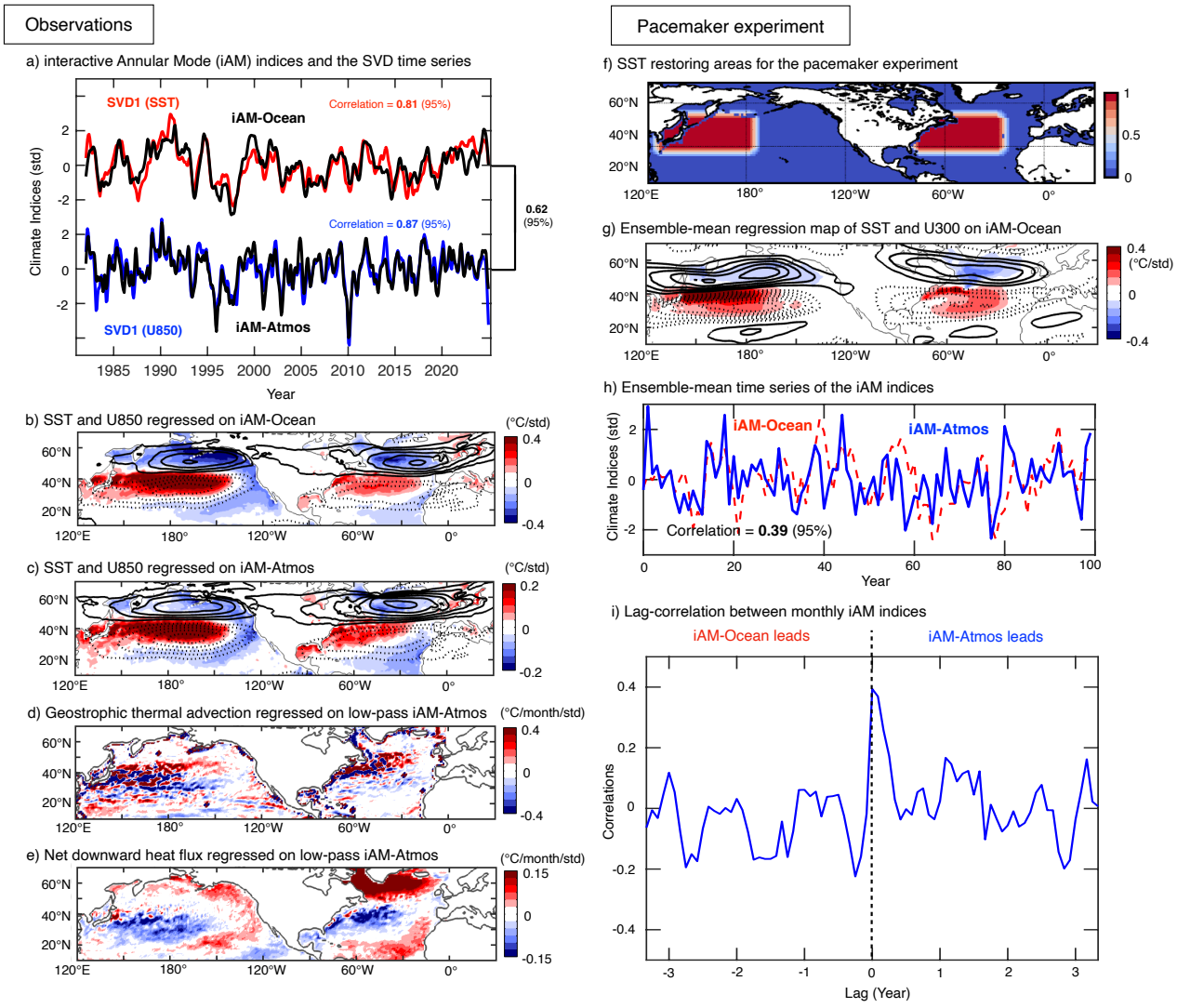

FIG. 4. **The interactive Annular Mode (iAM) and its coupling mechanism.** (a): Top, The standardized iAM-Ocean index (black) defined using regional-mean SST anomalies in the manner of the southern belt (35°N-45°N, 120°E-0°W) minus the northern belt (45°N-55°N, 120°E-0°W). Also shown is the SVD1 time series obtained from SST (red) as shown in Fig. 2d. Five-month running-mean filtering is applied. Bottom, As in top, but for the iAM-Atmos index defined using U850 in the manner of the northern belt minus the southern belt, and the SVD1 time series from U850 (blue). (b) Regression map of SST (shaded areas) and U850 (contours) onto the iAM-Ocean index. Contour interval is 0.2 m/s, and zero contours are omitted. (c) As in (b), but for the iAM-Atmos index. Contour interval is 0.4 m/s. (d, e): Regression map of (d) geostrophic thermal advection and (e) net downward heat flux on the one-year low-pass filtered iAM-Atmos index. (f): SST restoring areas for the pacemaker experiment. The factor shown in color is applied to the nudging heat flux at each grid point. (g): As in (b), but for the ensemble-mean SST and U300 from the pacemaker run. Contour interval is 0.1 m/s. (h): Ensemble-mean, annual-mean, standardized iAM-Ocean and iAM-Atmos indices from the pacemaker run. (i): Lag correlations between ensemble-mean monthly iAM-indices. Positive lag indicates that iAM-Atmos leads iAM-Ocean, and vice versa.

how these findings inform our understanding of midlatitude extreme weather in a warming world.

a. The iAM indices

The leading SVD mode of zonal wind described in the previous section represents the meridional migrations of the atmospheric jet stream. To characterize this variability, we define an index as the difference between regional-mean zonal wind anomalies in the manner of the northern belt (45°N-55°N, 120°E-0°W) minus the southern belt (35°N-45°N, 120°E-0°W). This index exhibits a correlation of 0.87 (significant at 95 %) with the SVD1 time series of zonal wind (Fig 4a, bottom). We designate this

index as the atmospheric component of iAM (the iAM-Atmos index), analogous to using the Southern Oscillation index as the atmospheric component of ENSO. The sign convention of the iAM-Atmos index is aligned with the conventional NAM index.

The oceanic component of iAM (the iAM-Ocean index) is defined similarly using the meridional difference of SST anomalies for the same regions. To ensure positive correlation with the iAM-Atmos index, we compute the meridional difference of the regional-mean SST anomalies in the opposite manner to the zonal wind: the southern belt (35°N-45°N, 120°E-0°W) minus the northern belt (45°N-55°N, 120°E-0°W). The iAM-Ocean index exhibit a correlation of 0.81 (significant at 95 %) with the SVD1 time series of SST (Fig 4a, top), serving a role analogous to the Niño 3.4 index for the oceanic component of ENSO. We note that the sign convention of the iAM-Ocean index is opposite to that of the conventional PDV index.

The meridional migrations of SST anomalies and the atmospheric jet stream demonstrate strong phase coherence. The two iAM indices show significant correlation at the 95% confidence level, each explaining approximately 40% of the other's variance (Fig. 4a). Regression maps of SST and zonal wind onto the iAM indices (Figs. 4b and 4c) reveal annular-shaped anomaly patterns that clearly capture the coordinated meridional migrations of both the atmospheric jet stream and SST. The high similarity between these spatial patterns suggests that the two iAM indices represent essentially the same physical mode of variability manifested in both oceanic and atmospheric fields.

b. Bidirectional coupling mechanisms between atmospheric and oceanic components of iAM

Based on multiple lines of evidence from previous studies, we could reasonably assume that the iAM-Atmos variability is capable of driving the iAM-Ocean variability. Western boundary currents are fundamentally wind-driven circulations (Stommel 1948), with their strength modulated to maintain mass balance against the southward Sverdrup transport mediated by wind. In the Pacific, studies of PDV have demonstrated that the Aleutian Low shapes SST patterns in the Kuroshio Extension region (e.g., Wallace et al. 1992; Newman et al. 2016). Similarly, in the Atlantic, atmospheric phenomena such as the North Atlantic Oscillation influence SST structure in the North Atlantic region (e.g., Visbeck et al. 1998, 2003).

Heat budget analysis near the ocean surface provides robust evidence for this dynamical relationship. Figure 4d shows the regression map of thermal advection by oceanic geostrophic currents onto the low-pass filtered iAM-Atmos index. This regression pattern exhibits the classical mechanism in which jet stream migrations associated with iAM-Atmos modulate western boundary current strength and subsequent heat transport from subtropical regions. While weaker in magnitude than the dynamic mechanism described above, thermodynamic processes act to relax these dynamically-induced SST anomalies. Figure 4e presents the regression map of net downward heat flux, analogous to that shown in Fig. 4d. During positive iAM-Atmos phases, the warm SST enhances surface latent and sensible heat release in the southern belt region, with the opposite occurring during negative phases.

The reciprocal influence (i.e., whether iAM-Ocean variability can drive iAM-Atmos variability) requires more careful investigation. To address this question, we have conducted a high-resolution pacemaker experiment where SSTs in the two boundary current regions are constrained by SST output from the preindustrial control run (Fig. 4f). This experimental design effectively prescribes the iAM-Ocean index variations, allowing us to interpret the ensemble-mean field as the climate system's response to iAM-Ocean variability (*see also* Data and Methods).

Results from our pacemaker experiment demonstrate that anomalously warm midlatitude oceans drive northward jet stream displacement. The regression map of ensemble-mean SST and zonal wind against the iAM-Ocean index (Fig. 4g) shows that prescribed SST variability in western boundary current regions generates an atmospheric response characteristic of annular modes. This response is consistent with Ogawa et al. (2012), who used an idealized atmospheric general circulation model (AGCM) to demonstrate that midlatitude SST fronts can anchor jet stream latitude. Additional evidence comes from Omrani et al. (2019), who revealed through more realistic AGCM experiments that western boundary currents amplify NAM variability. Both studies show that SST front-induced latent and sensible heating enhances baroclinicity, which modulates the jet stream position. This mechanism is consistent with the thermodynamic evidence shown in Fig. 4e.

The response of the iAM-Atmos index shows moderate but statistically significant temporal correlation with the prescribed iAM-Ocean index. Figure 4h illustrates the forced iAM-Atmos response to iAM-Ocean variability in the pacemaker experiment, revealing generally in-phase behavior with a significant correlation of 0.39. Lag correlation analysis between the time series indicates near-simultaneous variation relative to the phenomenon's interannual to decadal timescale (Fig. 4i), consistent with rapid atmospheric adjustment to SST front-induced heating.

c. Positive feedback loop and mathematical representation of iAM

The evidence presented in the previous subsection collectively demonstrate that positive iAM-Atmos (iAM-Ocean) anomalies actively generate positive iAM-Ocean (iAM-Atmos) responses, establishing a positive feedback loop. This coupled interaction produces air-sea coupled instability, enabling iAM to emerge as a dominant mode of

midlatitude climate system variance. The feedback mechanism parallels the Bjerknes feedback in the equatorial region that amplifies ENSO dominance in the tropical Pacific variability.

The positive feedback mechanism between iAM-Atmos and iAM-Ocean can be represented by a simplified coupled system of ordinary differential equations:

$$\frac{dI_A}{dt} = -\gamma_A I_A + \alpha_A I_O + F_A(t) \quad (1)$$

$$\frac{dI_O}{dt} = -\gamma_O I_O + \alpha_O I_A + F_O(t) \quad (2)$$

where I_A and I_O represent the iAM-Atmos and iAM-Ocean indices, respectively; γ_A and γ_O are the damping coefficients characterizing the intrinsic decay timescales; α_A and α_O are the coupling coefficients quantifying the strength of ocean-to-atmosphere and atmosphere-to-ocean feedbacks; and $F_A(t)$ and $F_O(t)$ denote external forcings. When $\alpha_A\alpha_O > \gamma_A\gamma_O$, the system exhibits unstable growth with an e-folding timescale of $\tau \sim (\gamma_A + \gamma_O)/(\alpha_A\alpha_O - \gamma_A\gamma_O)$ during the transient phase before nonlinearities become significant[1].

While the atmospheric response amplitude and correlation in the pacemaker experiment are weaker than observed in reanalysis (Fig. 4b), this difference reflects the experiment's prescribed, non-interactive iAM-Ocean variability. In the real world, the nonlinearity of the atmosphere-ocean system obscures the theoretically predicted unstable growth, so the proposed mathematical framework warrants further investigation. Nevertheless, multiple lines of evidence such as the idealized model (*see also* Fig. 1b), SVD analysis of observations (Figs. 2 and 3), heat budget analysis and global climate model experiments (Fig. 4) consistently provide a possible explanation for why the iAM variability emerges as a dominant mode as discussed in Section 3.

d. Implications for midlatitude extreme weather in a changing climate

The iAM-Ocean index exhibits a pronounced upward trend (Fig. 5a), consistent with enhanced warming signals observed in western boundary current regions relative to the global average (Wu et al. 2012). This positive trend underscores the immediate implications of iAM for anticipating climate change impacts on human society. The regression map of 2-meter air temperature onto the detrended iAM-Ocean index (Fig. 5b) reveals that iAM-associated jet stream fluctuations drive air temperature variations across densely populated regions of the Northern Hemisphere. These surface temperature patterns align with established NAM responses (Thompson and Wallace 1998, 2001), but our focus on low-frequency variability driven by air-sea interactions suggests enhanced predictability of iAM-Atmos compared to internal atmospheric dynamics alone, which has limited predictable timescale on o(10-100) days.

The sustained positive phase of iAM since 2020 exemplifies the significance of prolonged positive iAM events on multiyear timescales. Analysis of the Northern Hemisphere midlatitudes shows persistently high iAM values during this period (Fig. 5a; *see also* Fig. 1a), likely contributing to the warming trend observed across these regions. The record-breaking heat wave of 2024 occurred within this context of elevated iAM values. Comparing the observed 2024 air temperature pattern (Fig. 5c) with the positive iAM signature predicted by linear regression (Fig. 5b) reveals striking similarities, suggesting that the prolonged positive iAM state may have set favorable background conditions for this extreme event. Given the positive trend and substantial low-frequency power in the iAM-Ocean index, such background conditions conducive to extreme heat events are likely to become more common over the next decade.

5. Conclusions

In this study, we have demonstrated that a significant portion of low-frequency variance in the conventional NAM and PDV are explained by a coupled air-sea system, which we refer to as iAM. This mode is characterized by synchronized meridional migrations of SST anomalies and the atmospheric jet stream, manifesting as the leading SVD mode between SST and lower tropospheric zonal wind. While the oceanic component resembles PDV, it is rotated 45° toward the SST front variability mode in the data space of two leading PCs. The atmospheric component essentially represents an equal-weight combination of NAM and PNA. The system undergoes exponential growth through a positive feedback loop driven by air-sea coupled instability, establishing iAM as a dominant physical mode in the Northern Hemisphere (north of 20 ° N).

The physical mechanism underlying this instability, summarized in Fig. 5d, proceeds as follows. During positive iAM events, the northward-shifted jet stream induces dynamical ocean heating in the Gulf Stream and Kuroshio Extension regions. This heating manifests as wind stress variations over the ocean basin, enhancing warm advection through intensified western boundary currents. The resulting warm SST anomalies amplify surface latent and sensible heat releases, which enhance atmospheric baroclinicity and further displace the jet stream northward.

[1]The instability condition is derived from the eigenvalue equation of the linearized system. Setting the forcing terms to zero, we obtain the characteristic equation $\lambda^2 + (\gamma_A + \gamma_O)\lambda + \gamma_A\gamma_O - \alpha_A\alpha_O = 0$. The eigenvalues are $\lambda_{1,2} = \left(-(\gamma_A + \gamma_O) \pm \sqrt{(\gamma_A - \gamma_O)^2 + 4\alpha_A\alpha_O}\right)/2$. When $\alpha_A\alpha_O > \gamma_A\gamma_O$, one eigenvalue becomes positive, causing unstable growth. For a weakly coupled condition, i.e., $0 < \alpha_A\alpha_O - \gamma_A\gamma_O \ll (\gamma_A + \gamma_O)^2$, the positive eigenvalue is approximated as $\lambda_+ \sim (\alpha_A\alpha_O - \gamma_A\gamma_O)/(\gamma_A + \gamma_O)$, yielding the e-folding timescale $\tau = 1/\lambda_+ \sim (\gamma_A + \gamma_O)/(\alpha_A\alpha_O - \gamma_A\gamma_O)$

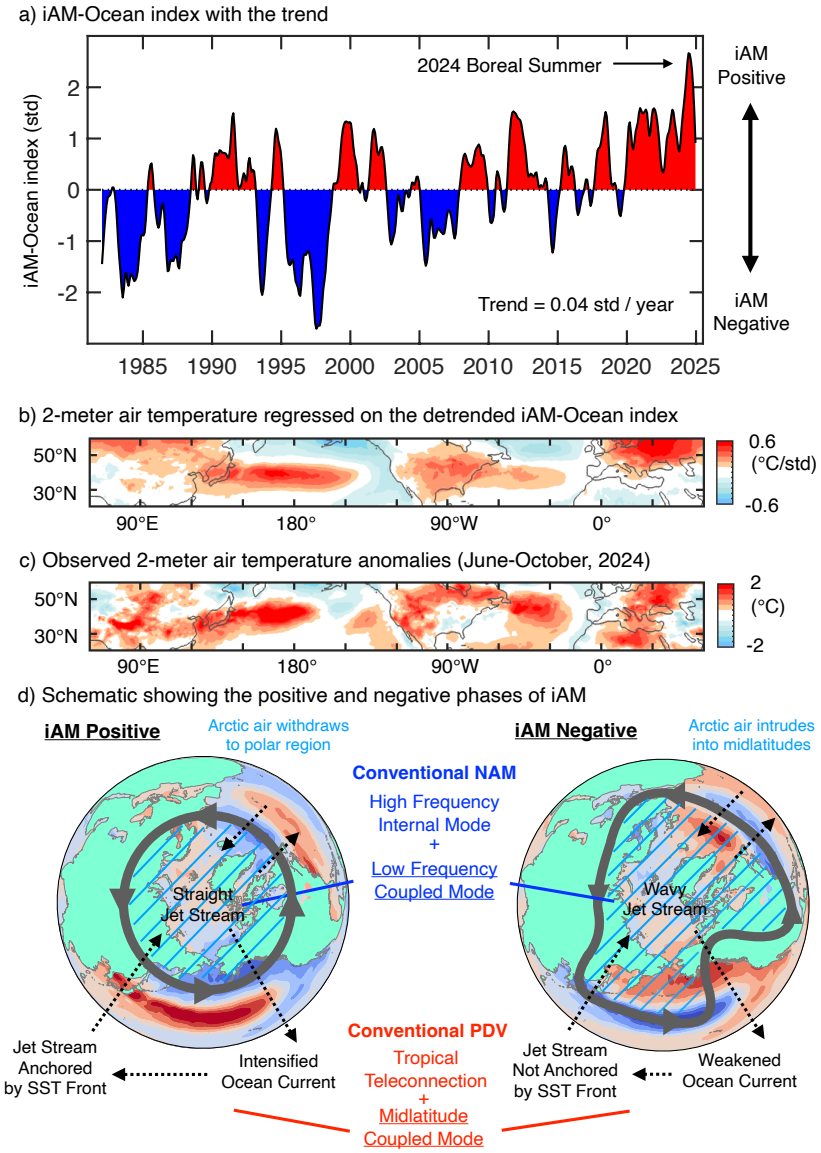

FIG. 5. **Implications of iAM for decadal Northern Hemispheric warmth.** (a): As in the top black curve in Fig. 4a, but the linear trend is retained. (b): As in Fig. 4b, but for 2-meter air temperature. (c): 2-meter air temperature anomalies averaged from June through October of 2024. (d): Schematic showing the positive feedback mechanism that amplifies the positive (left) and negative (right) iAM events. Their SST signatures are the same as in Fig. 4b, but the signs of the regression coefficients are reversed for the negative iAM.

During negative iAM events, the opposite processes lead to southward jet stream displacement and cool midlatitude SST anomalies.

The positive feedback mechanism underlying iAM bears a resemblance to the Bjerknes feedback that realizes ENSO variability in the tropics. While we have proposed the basic coupled dynamics of iAM based on observational evidence and a model experiment, the development of a comprehensive theoretical framework—analogous to the recharge oscillator (Jin 1997a,b) or delayed oscillator (Suarez and Schopf 1988; Battisti and Hirst 1989) theories for ENSO—remains a frontier for future research. Such theories would need to incorporate the unique characteristics of midlatitude dynamics, including the role of mesoscale eddies, the influence of basin geometry on western boundary current stability, and potential time-delayed negative feedbacks that could explain the quasi-periodic nature of iAM. The mathematical framework presented in Section 4 provides a starting point, but additional mechanisms governing phase transitions will be

crucial for developing a complete oscillator theory. Particularly important will be understanding how stratification changes and baroclinic adjustment processes might introduce time delays in the system, potentially supporting a self-sustained oscillatory behavior rather than merely exponential growth followed by nonlinear saturation.

It is a natural idea to look for a similar iAM mode in the Southern Hemisphere. Some previous studies investigated Southern Hemispheric intrinsic variability (Hogg and Blundell 2006; Hogg et al. 2022), and in fact, observational evidence shows that the Brazil current and the Agulhas return current are also synchronized (Kohyama et al. 2021a). Therefore, one may wonder if we could refer to it as the "Southern iAM". However, the SVD analysis reveals that, unlike its Northern Hemisphere counterpart where signals are largely confined to midlatitudes, the Southern Hemispheric SVD1 is fundamentally altered by tropical forcing. This tropical intrusion results in the Southern Hemisphere's western boundary current variability exhibiting shorter timescales (3-8 years), which is comparable to ENSO, distinguishing it from the longer timescales of the "Northern iAM" realized by slower internal dynamics in the midlatitudes due to the smaller Rossby deformation radius.

As a dominant mode of midlatitude low-frequency variability, iAM has significant implications for our changing climate, including the long-term forecasting of extreme heat events in densely populated regions. Furthermore, iAM variability impacts marine ecosystems through modulation of western boundary currents. Building upon established PDV-fisheries relationships (Mantua et al. 1997), iAM is expected to influence diverse marine species: from increased Atlantic cod mortality in warm Gulf Stream conditions (Pershing et al. 2015) to the migration patterns of Japanese sardine (Watanabe et al. 1996) and Pacific saury (Saitoh et al. 1986; Tian et al. 2003) in the Kuroshio region, where these species rely on specific conditions for spawning and nursery grounds (Kuroda et al. 2016). To advance our understanding of iAM behavior under anthropogenic forcing, we emphasize the critical need for enhanced midlatitude ocean observations and continued development of high-resolution global climate models.

Acknowledgments. During the preparation of this article, the authors have used Claude 3 only for English editing. After using this service, the authors reviewed and edited the content as needed, and the authors take full responsibility for the content of the publication. The first author is supported by Japan Society for the Promotion of Science (JSPS) KAKENHI Grant Numbers JP20K14554, JP22H04487, JP23H01241, and JP23K13169. The second author is supported by JSPS Kakenhi Grant Number JP20H05729, JP22K14098, and JP22H04487. The third author is supported by JSPS Kakenhi Grant Number JP20H05729, JP21K13997, JP22H04487, JP23K25946, JP23K25944, JP23K25935, JP24H00280, and JP24H02221. The fourth author is supported by JSPS KAKENHI Grant Number JP24H02229, and the Ministry of Environment of Japan Fund (JPMEERF20242001). The fifth author is supported by JSPS Kakenhi Grant Number JP23K25939. The first, second, third, and fourth authors are also supported by the Ministry of Education, Culture, Sports, Science and Technology (MEXT) program for the advanced studies of climate change projection (SENTAN) Grant Number JPMXD0722680395. We are grateful to Dr. Hiroaki Tatebe for providing the MIROC6-subhires model and its basic output, to Dr. John M. Wallace for useful advice on the phase diagram analysis, and to the anonymous reviewers for their time and constructive comments on our manuscript.

References

Ambaum, M. H., B. J. Hoskins, and D. B. Stephenson, 2001: Arctic oscillation or North Atlantic oscillation? *J. Climate*, **14 (16)**, 3495–3507.

Barnes, E. A., 2013: Revisiting the evidence linking Arctic amplification to extreme weather in midlatitudes. *Geophys. Res. Lett.*, **40 (17)**, 4734–4739.

Battisti, D. S., and A. C. Hirst, 1989: Interannual variability in a tropical atmosphere–ocean model: Influence of the basic state, ocean geometry and nonlinearity. *J. Atmos. Sci.*, **46 (12)**, 1687–1712.

Bretherton, C. S., M. Widmann, V. P. Dymnikov, J. M. Wallace, and I. Bladé, 1999: The effective number of spatial degrees of freedom of a time-varying field. *J. Climate*, **12 (7)**, 1990–2009.

Chelton, D. B., and M. G. Schlax, 1996: Global observations of oceanic Rossby waves. *Science*, **272 (5259)**, 234–238.

Chester, M. V., S. Markolf, and B. Allenby, 2019: Infrastructure and the environment in the Anthropocene. *Journal of Industrial Ecology*, **23 (5)**, 1006–1015.

Cohen, J., L. Agel, M. Barlow, C. I. Garfinkel, and I. White, 2021: Linking Arctic variability and change with extreme winter weather in the United States. *Science*, **373 (6559)**, 1116–1121.

Deser, C., 2000: On the teleconnectivity of the "Arctic Oscillation ". *Geophys. Res. Lett.*, **27 (6)**, 779–782.

Dong, M., C. Sun, T. Wei, Z. Guo, W. Lou, Z. Song, and L. Shi, 2025: Pdo modulates co-occurring summertime marine heatwaves in the extratropical north pacific and atlantic. *J. Geophys. Res. Atmos.*, **130 (4)**, e2024JD042 143.

Eyring, V., S. Bony, G. A. Meehl, C. A. Senior, B. Stevens, R. J. Stouffer, and K. E. Taylor, 2016: Overview of the Coupled Model Intercomparison Project Phase 6 (CMIP6) experimental design and organization. *Geosci. Model Dev.*, **9**, LLNL–JRNL–736 881.

Gallego, B., and P. Cessi, 2001: Decadal variability of two oceans and an atmosphere. *J. Climate*, **14 (13)**, 2815–2832.

Gasparrini, A., and Coauthors, 2015: Mortality risk attributable to high and low ambient temperature: a multicountry observational study. *Lancet*, **386 (9991)**, 369–375.

Gillett, N., and J. Fyfe, 2013: Annular mode changes in the CMIP5 simulations. *Geophys. Res. Lett.*, **40 (6)**, 1189–1193.

GISTEMP Team, 2025: GISS Surface Temperature Analysis (GISTEMP), version 4. NASA Goddard Institute for Space Studies. URL http://data.giss.nasa.gov/gistemp/, accessed on February 2nd, 2025.

Hartmann, D. L., 2015: *Global physical climatology*, Vol. 103. Elsevier.

Hersbach, H., and Coauthors, 2020: The ERA5 global reanalysis. *Quart. J. Roy. Meteor. Soc.*, **146 (730)**, 1999–2049.

Hogg, A. M., T. Penduff, S. E. Close, W. K. Dewar, N. C. Constantinou, and J. Martínez-Moreno, 2022: Circumpolar variations in the chaotic nature of Southern Ocean eddy dynamics. *J. Geophys. Res. Ocean*, **127 (5)**, e2022JC018 440.

Hogg, A. M. C., and J. R. Blundell, 2006: Interdecadal variability of the Southern Ocean. *J. Phys. Oceanogr.*, **36 (8)**, 1626–1645.

Holton, J. R., and G. J. Hakim, 2013: *An introduction to dynamic meteorology*, Vol. 88. Academic press.

Honda, Y., and Coauthors, 2014: Heat-related mortality risk model for climate change impact projection. *Environ. Health Prev. Med.*, **19**, 56–63.

Horel, J. D., and J. M. Wallace, 1981: Planetary-scale atmospheric phenomena associated with the Southern Oscillation. *Mon. Wea. Rev.*, **109 (4)**, 813–829.

Hoskins, B. J., and P. J. Valdes, 1990: On the existence of storm-tracks. *J. Atmos. Sci.*, **47 (15)**, 1854–1864.

Huang, B., C. Liu, V. Banzon, E. Freeman, G. Graham, B. Hankins, T. Smith, and H.-M. Zhang, 2021: Improvements of the daily optimum interpolation sea surface temperature (DOISST) version 2.1. *J. Climate*, **34 (8)**, 2923–2939.

Jin, F.-F., 1997a: An equatorial ocean recharge paradigm for ENSO. Part I: Conceptual model. *J. Atmos. Sci.*, **54 (7)**, 811–829.

Jin, F.-F., 1997b: An equatorial ocean recharge paradigm for ENSO. Part II: A stripped-down coupled model. *J. Atmos. Sci.*, **54 (7)**, 830–847.

Kido, S., M. Nonaka, and Y. Miyazawa, 2022: JCOPE-FGO: an eddy-resolving quasi-global ocean reanalysis product. *Ocean Dyn.*, **72 (8)**, 599–619.

Kimoto, M., F.-F. Jin, M. Watanabe, and N. Yasutomi, 2001: Zonal—eddy coupling and a neutral mode theory for the Arctic Oscillation. *Geophys. Res. Lett.*, **28 (4)**, 737–740.

Kohyama, T., H. Miura, and S. Kido, 2021a: Intensive Variability Extraction. *SOLA*, **17**, 246–250.

Kohyama, T., Y. Yamagami, H. Miura, S. Kido, H. Tatebe, and M. Watanabe, 2021b: The gulf stream and kuroshio current are synchronized. *Science*, **374 (6565)**, 341–346.

Kuroda, H., and Coauthors, 2016: Recent advances in Japanese fisheries science in the Kuroshio-Oyashio region through development of the FRA-ROMS ocean forecast system: Overview of the reproducibility of reanalysis products. *Open J. Marine Sci.*, **7 (01)**, 62.

Lenssen, N., G. A. Schmidt, M. Hendrickson, P. Jacobs, M. J. Menne, and R. Ruedy, 2024: A NASA GISTEMPv4 observational uncertainty ensemble. *J. Geophys. Res. Atmos.*, **129 (17)**, e2023JD040 179.

Limpasuvan, V., and D. L. Hartmann, 2000: Wave-maintained annular modes of climate variability. *J. Climate*, **13 (24)**, 4414–4429.

Lobell, D. B., W. Schlenker, and J. Costa-Roberts, 2011: Climate trends and global crop production since 1980. *Science*, **333 (6042)**, 616–620.

Mantua, N. J., S. R. Hare, Y. Zhang, J. M. Wallace, and R. C. Francis, 1997: A Pacific interdecadal climate oscillation with impacts on salmon production. *Bull. Amer. Meteor. Soc.*, **78 (6)**, 1069–1080.

Masson-Delmotte, V., and Coauthors, 2021: Climate change 2021: the physical science basis. *Contribution of working group I to the sixth assessment report of the intergovernmental panel on climate change*, **2 (1)**, 2391.

Masunaga, R., H. Nakamura, H. Kamahori, K. Onogi, and S. Okajima, 2018: JRA-55CHS: An Atmospheric Reanalysis Produced with High-Resolution SST. *SOLA*, **14**, 6–13.

Minobe, S., 1997: A 50–70 year climatic oscillation over the North Pacific and North America. *Geophys. Res. Lett.*, **24 (6)**, 683–686.

Minobe, S., A. Kuwano-Yoshida, N. Komori, S.-P. Xie, and R. J. Small, 2008: Influence of the Gulf Stream on the troposphere. *Nature*, **452 (7184)**, 206.

Nakamura, H., A. Isobe, S. Minobe, H. Mitsudera, M. Nonaka, and T. Suga, 2015: “Hot Spots” in the climate system—new developments in the extratropical ocean–atmosphere interaction research: a short review and an introduction. *J. Oceanogr.*, **71 (5)**, 463–467.

Newman, M., and Coauthors, 2016: The Pacific decadal oscillation, revisited. *J. Climate*, **29 (12)**, 4399–4427.

Ogawa, F., H. Nakamura, K. Nishii, T. Miyasaka, and A. Kuwano-Yoshida, 2012: Dependence of the climatological axial latitudes of the tropospheric westerlies and storm tracks on the latitude of an extratropical oceanic front. *Geophys. Res. Lett.*, **39 (5)**.

Omrani, N.-E., F. Ogawa, H. Nakamura, N. Keenlyside, S. W. Lubis, and K. Matthes, 2019: Key role of the ocean western boundary currents in shaping the northern hemisphere climate. *Sci. Rep.*, **9 (1)**, 3014.

Paul, A., and C. Schäfer-Neth, 2003: Modeling the water masses of the Atlantic Ocean at the Last Glacial Maximum. *Paleoceanogr.*, **18 (3)**.

Pershing, A. J., and Coauthors, 2015: Slow adaptation in the face of rapid warming leads to collapse of the Gulf of Maine cod fishery. *Science*, **350 (6262)**, 809–812.

Quadrelli, R., and J. M. Wallace, 2004: A simplified linear framework for interpreting patterns of Northern Hemisphere wintertime climate variability. *J. Climate*, **17 (19)**, 3728–3744.

Rasmusson, E. M., and J. M. Wallace, 1983: Meteorological aspects of the El nino/southern oscillation. *Science*, **222 (4629)**, 1195–1202.

Ray, D. K., P. C. West, M. Clark, J. S. Gerber, A. V. Prishchepov, and S. Chatterjee, 2019: Climate change has likely already affected global food production. *PLOS ONE*, **14 (5)**, e0217 148.

Ring, M. J., and R. A. Plumb, 2007: Forced annular mode patterns in a simple atmospheric general circulation model. *J. Atmos. Sci.*, **64 (10)**, 3611–3626.

Saitoh, S.-i., S. Kosaka, and J. Iisaka, 1986: Satellite infrared observations of Kuroshio warm-core rings and their application to study of

Pacific saury migration. *Deep Sea Res. Part A. Oceanogr. Res. Pap.*, **33 (11-12)**, 1601–1615.

Sanders, F., 1986: Explosive cyclogenesis in the west-central North Atlantic Ocean, 1981–84. Part I: Composite structure and mean behavior. *Mon. Wea. Rev.*, **114 (10)**, 1781–1794.

Screen, J. A., and I. Simmonds, 2014: Amplified mid-latitude planetary waves favour particular regional weather extremes. *Nat. Clim. Change*, **4 (8)**, 704–709.

Shapiro, M. A., and D. Keyser, 1990: *Fronts, jet streams and the tropopause*. Springer.

Stommel, H., 1948: The westward intensification of wind-driven ocean currents. *Eos, Transactions American Geophysical Union*, **29 (2)**, 202–206.

Suarez, M. J., and P. S. Schopf, 1988: A delayed action oscillator for ENSO. *J. Atmos. Sci.*, **45 (21)**, 3283–3287.

Tatebe, H., and Coauthors, 2019: Description and basic evaluation of simulated mean state, internal variability, and climate sensitivity in MIROC6. *Geosci. Model Dev.*, **12 (7)**, 2727–2765.

Thompson, D. W., and J. M. Wallace, 1998: The Arctic Oscillation signature in the wintertime geopotential height and temperature fields. *Geophys. Res. Lett.*, **25 (9)**, 1297–1300.

Thompson, D. W., and J. M. Wallace, 2001: Regional climate impacts of the Northern Hemisphere annular mode. *Science*, **293 (5527)**, 85–89.

Tian, Y., T. Akamine, and M. Suda, 2003: Variations in the abundance of Pacific saury (Cololabis saira) from the northwestern Pacific in relation to oceanic-climate changes. *Fisheries research*, **60 (2-3)**, 439–454.

Visbeck, M., E. P. Chassignet, R. G. Curry, T. L. Delworth, R. R. Dickson, and G. Krahmann, 2003: The ocean's response to North Atlantic Oscillation variability. *Geophys. Monogr. Amer. Geophys. Union*, **134**, 113–146.

Visbeck, M., H. Cullen, G. Krahmann, and N. Naik, 1998: An ocean model's response to North Atlantic Oscillation-like wind forcing. *Geophys. Res. Lett.*, **25 (24)**, 4521–4524.

Vlock, L., and P. Jacobs, 2025: Temperatures Rising: NASA Confirms 2024 Warmest Year on Record. URL https://www.nasa.gov/news-release/temperatures-rising-nasa-confirms-2024-warmest-year-on-record/, accessed on February 2nd, 2025.

Wallace, J. M., 2000: North Atlantic Oscillation/Annular Mode: two paradigms—one phenomenon. *Quart. J. Roy. Meteor. Soc.*, **126 (564)**, 791–805.

Wallace, J. M., C. Smith, and C. S. Bretherton, 1992: Singular value decomposition of wintertime sea surface temperature and 500-mb height anomalies. *J. Climate*, **5 (6)**, 561–576.

Watanabe, M., and F.-F. Jin, 2004: Dynamical prototype of the Arctic Oscillation as revealed by a neutral singular vector. *J. Climate*, **17 (11)**, 2119–2138.

Watanabe, Y., H. Zenitani, and R. Kimura, 1996: Offshore expansion of spawning of the Japanese sardine, Sardinops melanostictus, and its implication for egg and larval survival. *Can. J. Fish. Aquat. Sci.*, **53 (1)**, 55–61.

Wills, R. C., T. Schneider, J. M. Wallace, D. S. Battisti, and D. L. Hartmann, 2018: Disentangling global warming, multidecadal variability, and El Niño in Pacific temperatures. *Geophys. Res. Lett.*, **45 (5)**, 2487–2496.

Wu, L., and Coauthors, 2012: Enhanced warming over the global subtropical western boundary currents. *Nature Climate Change*, **2 (3)**, 161–166.

Yamagami, Y., H. Tatebe, T. Kohyama, S. Kido, and S. Okajima, 2025: Gulf stream drives kuroshio behind the recent abnormal ocean warming. *arXiv preprint arXiv:2503.01117*.

Yamamoto, M., T. Oba, J. Shimamune, and T. Ueshima, 2004: Orbital-scale anti-phase variation of sea surface temperature in mid-latitude North Pacific margins during the last 145,000 years. *Geophys. Res. Lett.*, **31 (16)**.

Yasuda, Y., and T. Kohyama, 2025: A mechanism of stochastic synchronization in the climate system: an interpretation of the boundary current synchronization as a maxwell's demon. *arXiv preprint arXiv:2408.01133*.

Young, G. S., and T. D. Sikora, 2003: Mesoscale stratocumulus bands caused by Gulf Stream meanders. *Mon. Wea. Rev.*, **131 (9)**, 2177–2191.

Zhang, R., 2008: Coherent surface-subsurface fingerprint of the Atlantic meridional overturning circulation. *Geophys. Res. Lett.*, **35 (20)**.

Zhang, Y., S.-P. Xie, Y. Kosaka, and J.-C. Yang, 2018: Pacific decadal oscillation: Tropical Pacific forcing versus internal variability. *J. Climate*, **31 (20)**, 8265–8279.